Electrodeposition of bismuth at a graphene modified carbon electrode and its application as an easily regenerated sensor for the electrochemical determination of the antimicrobial drug metronidazole☆

Tian Yu [a], Luke Glennon [a], Orla Fenelon [a], Carmel B. Breslin [a,b,*]

[a] Department of Chemistry, Maynooth University, Maynooth, Co. Kildare, Ireland
[b] Kathleen Lonsdale Institute for Human Health Research, Maynooth University, Maynooth, Co. Kildare, Ireland

ABSTRACT

Metronidazole is a well-known antimicrobial drug that belongs to the nitroimidazole family of antibiotics. It has been widely used in the treatment of infections, but its accumulation in aquatic environments is an emerging concern. In this study a glassy carbon electrode was modified with graphene (Gr) nanoplatelets and bismuth. Both the Gr and Bi were electrochemically deposited onto the glassy carbon and the modified electrode was employed in the electrochemical detection of metronidazole. At the modified electrode, the reduction of metronidazole was found to be an adsorption-controlled reaction. The optimised sensor, which was fabricated within 6 min, exhibited good selectivity in the presence of various inorganic and organic compounds, good recovery in tap water, and exhibited a linear calibration curve extending from 0.005 to 260 μM, with a limit of detection of 0.9 nM. The sensor was easily regenerated through the simple oxidation of the Bi deposit followed by a 100 s reduction period in the Bi(III) solution to give a newly generated surface. Good reproducibility was achieved using this simple regeneration approach.

1. Introduction

Metronidazole (2-methyl-5-nitroimidazole-1-ethanol) (MTZ) belongs to the nitroimidazole family of antibiotics and it has been commonly used in the treatment of infections caused by bacteria such as helicobacter pylori [1], giardia lamblia and trichomonas vaginalis [2]. More recently, it has been used to treat oral and dental infections, respiratory tract infections and Crohn's disease [3]. It is an effective antimicrobial agent against anaerobic bacteria, with added antiparasitic properties, and it has been used extensively to treat infections in both humans [3] and animals [2]. Nevertheless, MTZ has genotoxic and mutagenic side effects [3]. Its accumulation in the aquatic environment is especially concerning as it can be hazardous to both humans and aquatic life. It has a very high solubility in water, and exhibits very good stability, with poor biodegradability, photo and hydrolytic breakdown, meaning that it can persist for considerable time in aquatic environments. Indeed, high levels of pharmaceuticals, including MTZ, have been detected in water supplies in urban areas [4], and these MTZ-contaminated sites are at a risk of proliferating antimicrobial

resistance. This has direct implications for the UN Sustainable Development Goal of clean water and sanitation.

Consequently, there is much interest in developing methods that can not only be employed in the determination of MTZ in biological media, but also in aquatic environments. Electrochemical sensors that are capable of detecting MTZ have several advantages over some of the more standard analytical techniques, such as high performance liquid chromatography. These include simplicity and portability with little sample preparation. Nevertheless, electrochemical sensors need to have high sensitivity and selectivity with good stability. Therefore, electrode surface modifiers are often employed and various MTZ sensors have been fabricated using this approach. Several carbon-based materials have been modified and employed, including carbon nanotubes in carbon pastes [5], carbon fibres [6], diamond [7], and graphene-modified sensors [8–10], including graphene modified with copper oxide nanoparticles [10], silver nanoparticles [11] and nickel manganous oxide nanoparticles [12]. For example, a sensor formed with dysprosium vanadate nanoparticles combined with oxidised carbon nanofibers [6] has been employed to give impressive detection with a limit of detection

in the nM region. While many of these sensors have very good analytical performances, they have time consuming synthetic steps [5,9], solution-based processing [6], with long drying periods [8]. In addition, there is little evidence to indicate that the surfaces can be easily regenerated or renewed.

As MTZ is typically reduced at applied potentials in the vicinity of −0.6 V to −0.8 V vs SCE, then electrodeposited or electroplated bismuth films may be suitable in its detection. Recently, bismuth films have been employed successfully using stripping voltammetry in the detection of heavy metal ions [13–15]. Simultaneous detection has been achieved at bismuth modified electrodes with Cd(II) and Pb(II) [16], Cd(II), Zn(II) and Pb(II) [17], and Cd(II) and Pb(II) [18]. While bismuth modified electrodes are normally used in the detection of heavy metal ions, they have more recently been successfully utilised in the electrochemical detection of nitrophenols [19,20], while bismuth oxides have been employed in the detection of paracetamol [21]. It has been suggested that bismuth is a good replacement for the well-known mercury electrodes, especially the dropping mercury electrode (DME), which possess a wide electrochemical window [22,23], but are no longer used due to environmental concerns. For example, it was shown by Hutton et al. [23] that electrodeposited Bi film electrodes have high hydrogen overpotentials and low background currents. Furthermore, bismuth is a non-toxic element. Indeed bismuth oxides have been suggested as contrast agents in X-ray computed tomography (CT) [24].

In this paper, we show that an electrodeposited bismuth film deposited onto a graphene modified glassy carbon electrode gives a simple and effective sensor for the electrochemical detection of MTZ. Furthermore, the sensor surface can be easily renewed by the simple oxidation and removal of the bismuth film, followed by its subsequent regeneration through electrochemical deposition.

2. Experimental

All chemicals, including bismuth nitrate pentahydrate, Bi (NO$_3$)$_3$5H$_2$O, metronidazole, phosphate and acetate salts, acetic acid, and graphene nanoplatelets, Gr (10 μm), were obtained from Sigma–Aldrich. All chemicals were of analytical grade reagents and used without any further purification. Cyclic voltammetry measurements were recorded using a Solartron 1287 potentiostat. The surface morphology was studied using scanning electron microscopy (SEM) with a Hitachi S-3200-N microscope, while energy dispersive X-ray analysis (EDX) was carried out using an Oxford Instrument INCAz-act ESX system. The UV–visible spectroscopy measurements were recorded using a Cary 50 spectrometer, while the FTIR measurements were performed using a Nicolet iS50 FTIR spectrometer.

A standard three-electrode cell was employed in all electrochemical measurements. A glassy carbon electrode (GCE), 3 mm in diameter, was utilised as the working electrode, a high surface area platinum wire served as the counter electrode, and a saturated calomel electrode (SCE) was employed as the reference. Unless otherwise stated, all potentials are provided with respect to the SCE reference electrode. The GCE was polished on a micro-cloth (Aka-Napel cloth) with progressively smaller sized diamond suspensions (Akasol) to a final 1 μm particle size, sonicated, thoroughly rinsed with deionised water and dried under a stream of air.

Unless otherwise stated, a 1.0 mM Bi(NO$_3$)$_3$5H$_2$O solution was prepared by initially dissolving 10 mM Bi(NO$_3$)$_3$5H$_2$O in 0.1 M HNO$_3$ to give complete dissolution without any insoluble hydroxides. This solution was then diluted with 0.1 M acetate buffer at a pH of 4.4 to give the 1.0 mM Bi(NO$_3$)$_3$5H$_2$O in 0.01 M HNO$_3$ and 0.09 M acetate with a final pH of 1.23. The suspension of Gr (5 mg ml^{-1}) was prepared by dispersing Gr nanoplatelets in a 0.1 M phosphate buffer (PBS) at a pH of 7.0 using ultrasonication. The bismuth modified GCE (GCE/Bi) was fabricated using the 1.0 mM bismuth nitrate solution by applying a constant potential of −1.0 V for 100 s. The Gr and bismuth modified GCE (GCE/Gr/Bi) was fabricated through successive electrodeposition of Gr and

bismuth. First, Gr was electrochemically deposited on the surface of GCE to form GCE/Gr by scanning for five cycles at a scan rate of 50 mV s^{-1} in the potential range from −1.5 V to 0.8 V vs SCE with magnetic stirring of the Gr dispersion. After electrodeposition, the prepared electrode, GCE/Gr, was washed with deionised water. Next, the GCE/Gr was immersed in 1.0 mM bismuth nitrate solution, and a constant potential of −1.0 V vs SCE was applied for 100 s to form GCE/Gr/Bi.

A stock solution of 4 mM MTZ was prepared in PBS buffer (0.1 M) at a pH of 7.0. The pH was varied between 3.5 and 13.0 by adding HNO$_3$ or NaOH to the 0.1 M PBS solution. Unless otherwise stated, the cyclic voltammetry (CV) experiments were performed at a scan rate of 50 mV s^{-1} in solutions deoxygenated for 20 min using high purity nitrogen gas.

3. Results and discussion

The GCE/Gr, GCE/Bi and GCE/Gr/Bi electrodes were formed, characterised and then employed in the electrochemical detection of MTZ. The corresponding results are described and discussed in the following sections.

3.1. Formation and characterisation of the modified electrodes

The reduction of Bi(III) at the GCE was carried out in acidified solutions, to prevent the formation of insoluble bismuth oxides/hydroxides. The reduction of Bi(III) can be described by Eq. (1), where the reduction potential is predicted to occur at 0.17 V with a 5.0 mM concentration. As shown in Fig. 1(a), the reduction of Bi(III) gives rise to an unsymmetrical reduction wave with a peak potential centred at approximately −0.17 V. This gives an overpotential of approximately 0.34 V. The corresponding oxidation wave is evident with a peak potential at about −0.10 V vs SCE and this peak is more symmetrical as the deposited bismuth is oxidised. It is clear from this voltammogram that the upper potential is limited by the oxidation of the deposited bismuth which begins at potentials in the vicinity of −0.20 V. Therefore, the voltammograms recorded for MTZ in PBS were cycled to an upper potential of −0.30 V vs SCE to prevent the oxidation of bismuth (as the oxidation of the deposited bismuth begins at potentials of about −0.30 V vs SCE when the GCE/Bi is placed in MTZ at a pH of 7.0.

$$Bi^{3+} + 3e^- \rightarrow Bi \quad E = 0.215 + 0.0197 \log[Bi(III)] \qquad 1$$
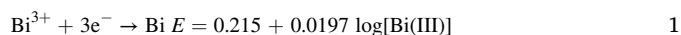
The voltammograms recorded with GCE, GCE/Gr, GCE/Bi and GCE/Gr/Bi are compared at a concentration of 0.1 mM MTZ in Fig. 1(b). It is obvious that the MTZ undergoes an irreversible redox reaction. The corresponding reduction reaction is summarised in Scheme 1, where the MTZ is reduced through a 4H$^+$/4e$^-$ transfer step to give the *N*-hydroxy amino compound [6]. On comparing the four electrodes, it is seen that the reduction of MTZ occurs at the highest overpotential at an applied potential of about −0.74 V vs SCE for the unmodified GCE with a very low peak current. A considerable reduction in the overpotential and a clear increase in the peak current is seen with the GCE/Bi. A further increase in the peak current is observed on the modification of GCE with Gr, and the highest peak current is seen with the GCE/Gr/Bi, with the peak potential at −0.64 V vs SCE and a peak current of 0.07 mA. Although the more thermodynamically favoured reduction of MTZ is seen with the GCE/Bi electrode, the highest peak current is obtained when the Bi is combined with the deposited Gr to give GCE/Gr/Bi. On comparing the GCE and GCE/Gr/Bi a 10-fold increase in the peak current is observed, clearly showing that the GCE/Gr/Bi has potential applications in the electrochemical detection of MTZ. Furthermore, the reproducibility of the MTZ detection was very good and this is illustrated in Table 1, where five separate experiments are shown for the GCE/Bi and GCE/Gr/Bi electrodes at a relatively high concentration of 2 mM and a lower concentration of 0.1 mM for the GCE/Gr/Bi. The % RSD values are low and well below 5%, indicating good reproducibility.

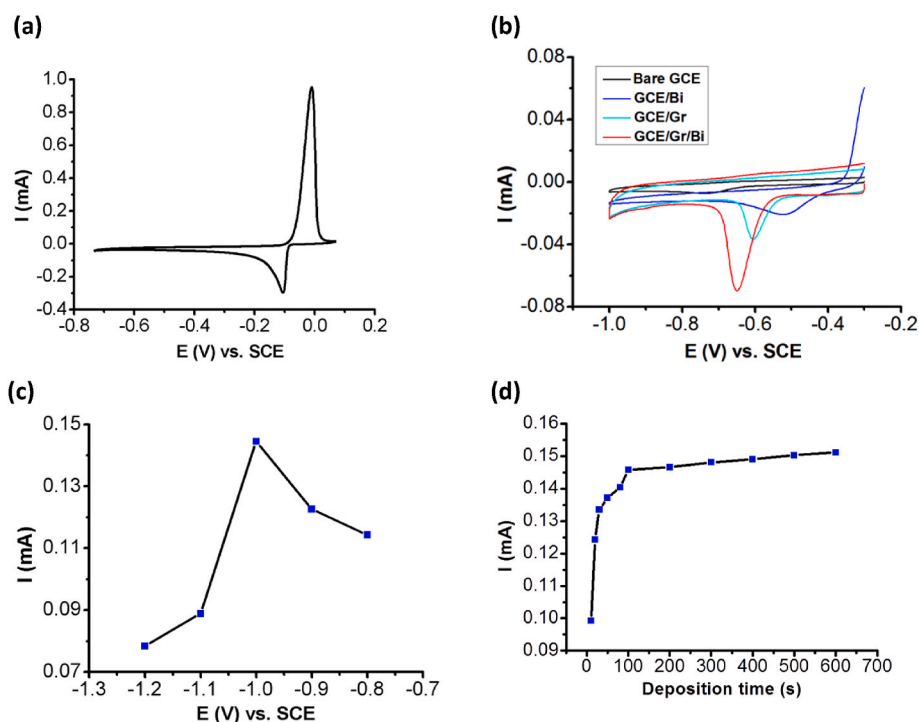The influence of the deposition time and potential on the

Fig. 1. (a) CV of GCE recorded in 5.0 mM Bi(NO$_3$)$_3$, **(b)** CVs of GCE, GCE/Bi, GCE/Gr and GCE/Gr/Bi recorded in 0.1 mM MTZ in PBS at 60 mV s^{-1}, **(c)** peak current of MTZ (2.0 mM) plotted as a function of the Bi deposition potentials (1.0 mM Bi(III) and deposition period of 100 s) for GCE/Bi and **(d)** peak current of MTZ (2.0 mM) plotted as a function of Bi deposition period at −1.0 V in 1.0 mM Bi(III).
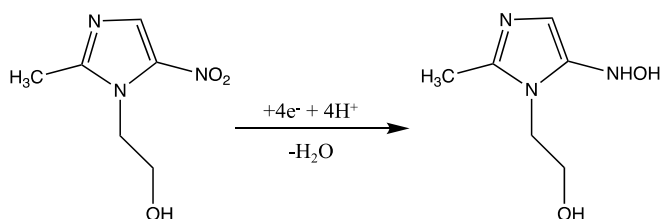
Scheme 1. Schematic illustrating the electrochemical reduction of MTZ, with the conversion of the –NO$_2$ to the –NHOH group.

Table 1
Reproducibility of GCE/Bi and GCE/Gr/Bi in the detection of MTZ.

	Reduction Peak Current (µA)					RSD (%) (n = 5)
	1	2	3	4	5	
GCE/Bi (2.0 mM MTZ)	147.3	143.9	143.5	144.6	147.0	1.22
GCE/Gr/Bi (2.0 mM MTZ)	278.3	274.5	273.6	277.5	276.8	0.73
GCE/Gr/Bi (0.1 mM MTZ)	69.53	69.75	69.93	69.14	69.48	0.43

performance of the GCE/Bi electrode in the electrochemical detection of 2.0 mM MTZ are summarised in Fig. 1(c) and (d). Here it is evident that the optimum electrodeposition potential is −1.0 V vs SCE. As the potential is varied from −0.8 V to −1.0 V vs SCE, there is an increase in the peak current for the reduction of MTZ. However, at potentials lower than −1.0 V vs SCE the reduction of bismuth is less effective, as the reduction of hydrogen ions occurs. Short deposition times, in the vicinity of 100 s, give rise to the optimum deposition period, in terms of both the sensor performance and fabrication time. There is no further increase in the MTZ reduction current for higher deposition times, Fig. 1(d). Deposition at −1.0 V vs SCE for 100 s gives a charge of (2.670 ± 0.003)

× 10^{-3} C. Assuming the charge is due to the reduction of Bi(III) and the competing reduction reactions are negligible, then approximately 1.93 µg of Bi is formed or deposited at the GCE.

SEM micrographs are shown for the GCE/Gr in Fig. 2 (a) and (b) and for GCE/Gr/Bi in Fig. 2(c) and (d). The Gr sheets are clearly evident in the low magnification SEM and are well dispersed over the entire surface, but with some evidence of aggregation at some sites. This is also evident in Fig. 2(b) with some Gr sheets stacked. Following the deposition of bismuth for 100 s, the micrographs show the bismuth deposited onto the Gr sheets and also on the free GCE surface, with the Bi deposits adopting nanowire like deposits with some larger particles. The EDX spectrum shows the presence of Bi, C and O, clearly indicating that the Bi is deposited at the electrode surface, Fig. 2(e). The presence of the oxygen is consistent with the oxygenated groups on the Gr, and possibly on the glassy carbon electrode. The mapping data for C and Bi, illustrated in Fig. 2(f), show that both the C and Bi are nearly evenly dispersed across the surface.

The electrodeposition of Gr clearly increases the surface area of the electrode. Using the [Fe(CN$_6$)]$^{3-/4-}$ redox probe with the unmodified GCE electrode, the electroactive surface area of the GCE electrode was estimated as 0.107 cm^2 using the linear regression equation $I(A) = 0.79 \times 10^{-4} \upsilon^{1/2} - 1.60 \times 10^{-6}$, R^2 = 0.999. A much higher electroactive surface area of 0.255 cm^2 was observed using a similar analysis with the GCE/Gr, indicating that on addition of the Gr, the electroactive surface area increases by approximately a factor of 2.4.

3.2. Influence of scan rate

The influence of scan rate on the peak current associated with the reduction of MTZ is shown in Fig. 3 (a), (b) and (c) for the GCE/Bi, GCE/Gr, and GCE/Gr/Bi, respectively, at a fixed concentration of 0.1 mM MTZ. On plotting the peak current as a function of the square root of the scan rate a linear plot was obtained for the GCE/Bi electrode, Fig. 3(d), with the linear regression equation, $I = 3.10 \times 10^{-3} \upsilon^{1/2} + 2.50 \times 10^{-3}$, R^2 = 0.999, where I is expressed as mA and υ in mV/s, indicating that the
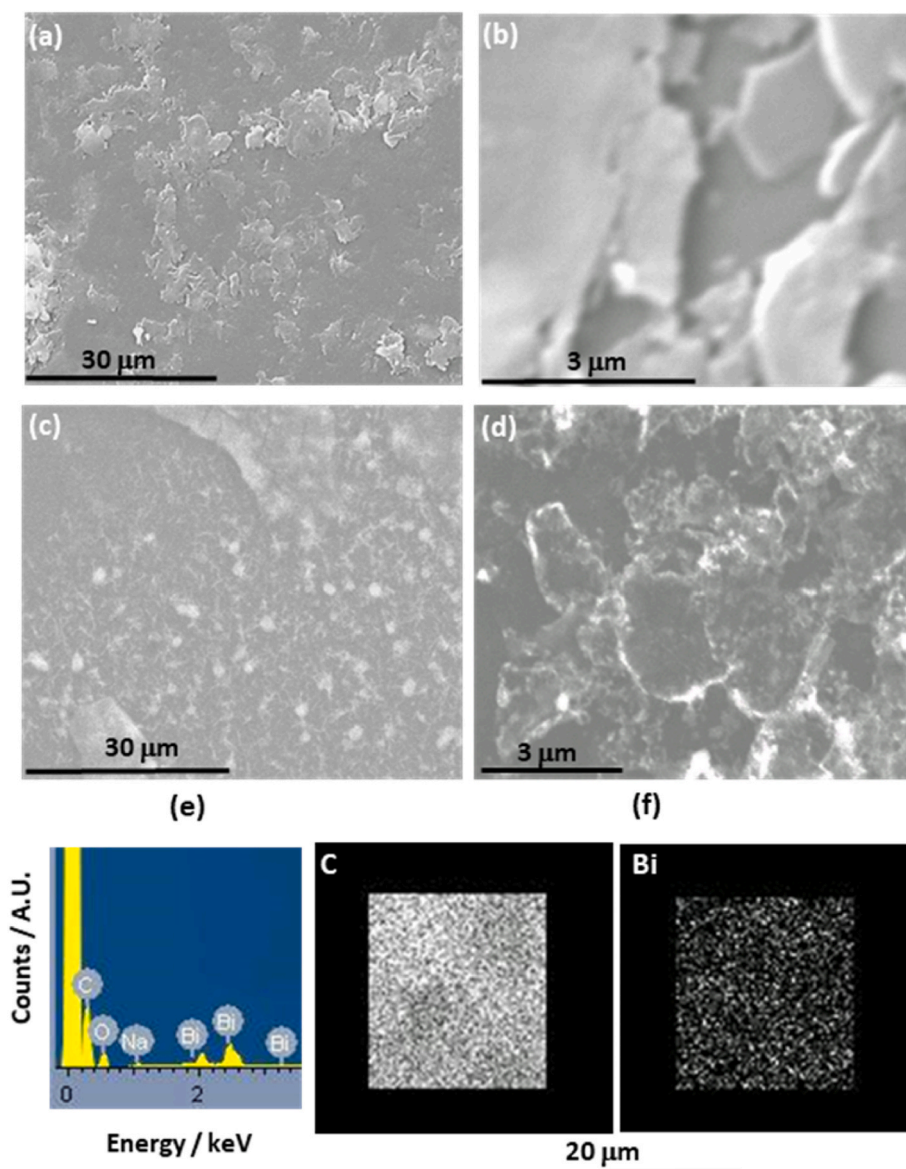
Fig. 2. SEM micrographs of **(a)** and **(b)** GCE modified with electrodeposited Gr, **(c)** and **(d)** GCE modified with electrodeposited Gr and Bi, **(e)** EDX spectrum recorded at GCE/Gr/Bi and **(f)** mapping of C and Bi at the GCE/Gr/Bi.

reduction of MTZ is under diffusion control. Similarly, the reduction of MTZ was under diffusion control at the unmodified GCE, with a linear regression equation of $I = 1.00 \times 10^{-3} \, v^{1/2} - 0.40 \times 10^{-3}$, $R^2 = 0.999$ (Fig. S1, supplementary data). However, the peak current was found to be related to the scan rate with both GCE/Gr, Fig. 3(e), and GCE/Gr/Bi, Fig. 3(f), which indicates that the reduction of MTZ becomes an adsorption controlled reaction when the Gr nanoplatelets were incorporated into the sensor. The linear regression equation for GCE/Gr was obtained as $I = 5.80 \times 10^{-4} \, v + 1.90 \times 10^{-3}$, with $R^2 = 0.999$, while the corresponding analysis gave the equation, $I = 1.24 \times 10^{-3} \, v + 4.0 \times 10^{-3}$, $R^2 = 0.999$ for GCE/Gr/Bi. Indeed, on plotting the logarithm of the peak current as a function of the logarithm of the scan rate, linear relationships were observed with slope values of 0.55 for GCE/Bi, and slope values in the vicinity of 1.0 for the GCE/Gr (0.92) and GCE/Gr/Bi (0.99) electrodes, clearly indicating that the reduction of MTZ changes from a diffusion-controlled reaction at the GCE/Bi to an adsorption controlled process when the Gr nanoplatelets are present. This suggests that the graphene sheets facilitate the adsorption of the MTZ. This was explored further, by using a combination of experiments designed to probe the adsorption process and these are summarised in Fig. 3(g), (h)

and (i). The data illustrated in Fig. 3(g) were recorded by first cycling the GCE/Gr/Bi in 0.1 mM MTZ, then the electrode was gently rinsed with deionised water and transferred to the PBS solution, and cycled in the absence of MTZ. In this case a clear reduction wave is seen, indicating a memory effect with the electrochemical reduction of the adsorbed MTZ. The influence of accumulation time is evident in Fig. 3(h), indicating that the optimum accumulation period is about 300 s, again consistent with adsorption of the MTZ in the presence of Gr. In Fig. 3(i), UV–visible spectra are presented showing the data recorded for 0.01 mM MTZ in the presence and absence of 10 mg Gr. In this case, a decrease in the absorbance is seen when Gr is added to the MTZ solution, indicating that the MTZ is removed from the solution phase by adsorbing onto the Gr. In summary, these data clearly show that the incorporated Gr within GCE/Gr/Bi facilitates the adsorption of MTZ.

The diffusion controlled reactions observed with GCE and GCE/Bi are governed by the Randles-Sevick equation, Eq. (4), where n_r corresponds to the total number of electrons transferred, n represents the number of electrons transferred in the rate-determining step, α is the charge transfer coefficient, D is the diffusion coefficient of MTZ, c represents the concentration and A is the surface area. The charge transfer
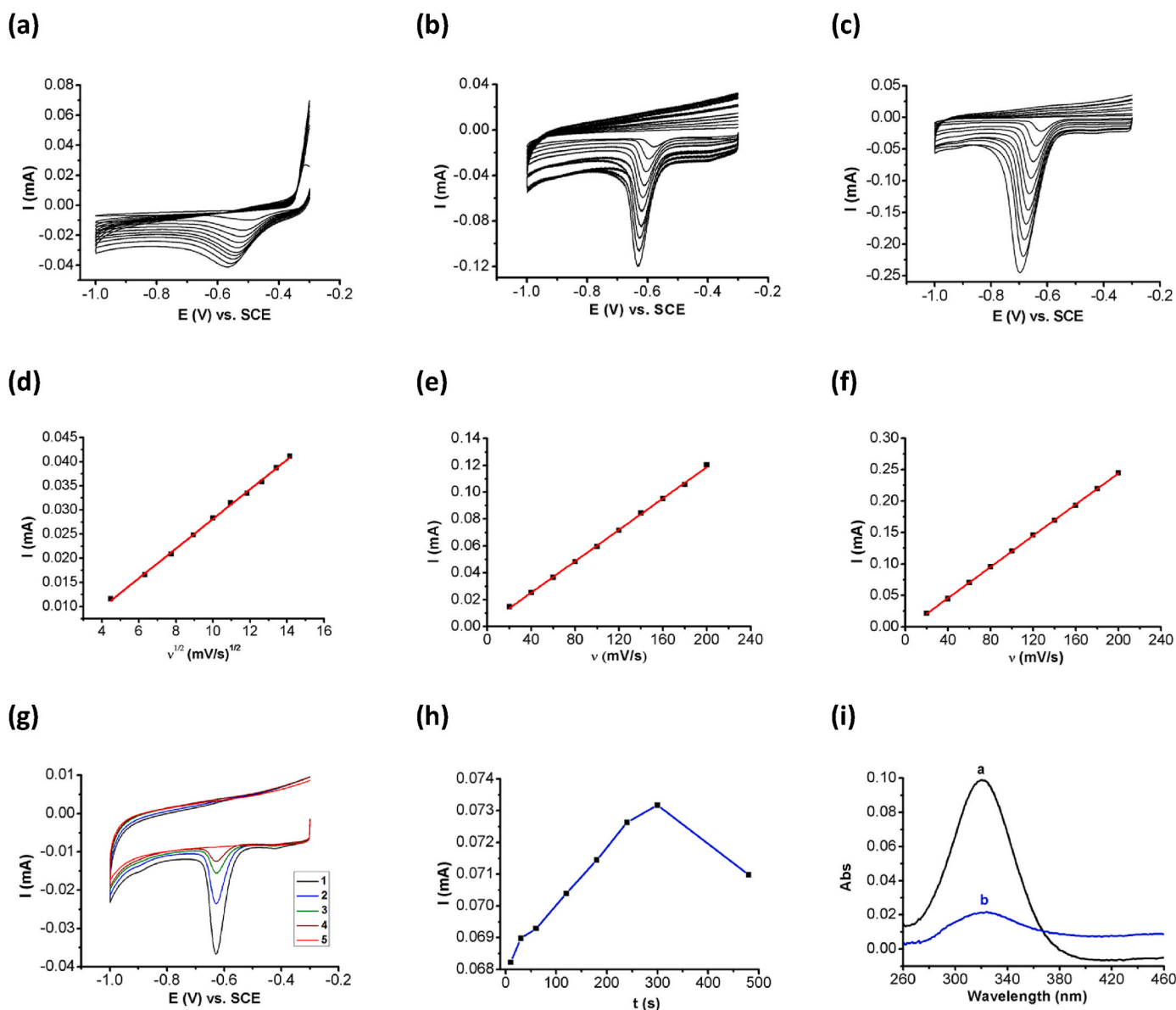
Fig. 3. CVs recorded in 0.1 mM MTZ at scan rates from 20 to 200 mV s^{-1} for **(a)** GCE/Bi, **(b)** GCE/Gr and **(c)** GCE/Gr/Bi, peak current plotted as a function of **(d)** square root of scan rate for GCE/Bi, **(e)** scan rate for GCE/Gr and **(f)** scan rate for GCE/Gr/Bi, **(g)** memory effects showing voltammograms 1, 2, 3, 4 and 5 recorded in the buffer in the absence of MTZ for GCE/Gr/Bi, **(h)** peak current as a function of immersion period for GCE/Gr/Bi and **(i)** UV–Vis spectrum of MTZ (0.01 mM) in the absence (a) and presence (b) of Gr (10 mg).

coefficient, α, was taken as 0.55, and n_r, which represents the total number of electrons transferred during the reduction step, was 4.0, Scheme 1. Normally, a single electron transfer step becomes the rate-determining step, as the simultaneous transfer of multiple electrons is highly improbable and therefore n was set to unity.

$$I = 2.99 \times 10^5 n_r (n\alpha)^{1/2} A c D^{1/2} \nu^{1/2} \qquad (4)$$

The diffusion coefficient of MTZ was estimated using Eq. (4) as 4.20 × 10^{-6} cm^2 s^{-1} for the unmodified GCE electrode. This estimated diffusion coefficient is in reasonably good agreement with the value reported by Ammar et al. [7] of 7.96 × 10^{-6} cm^2 s^{-1}. Using this computed diffusion coefficient and comparing the linear regression equations for the GCE and GCE/Bi, the surface area of GCE/Bi was estimated as 0.180 cm^2, an approximate 1.7-fold increase in the electroactive surface area after the electrodeposition of the Bi.

Using Eq. (5), where E_p and $E_{p1/2}$ are the peak and half-wave potentials, respectively, the $n\alpha$ value was estimated as 0.55 for GCE/Gr/Bi.

This is consistent with a one-electron transfer rate-determining step during the reduction of MTZ at GCE/Gr/Bi, as the simultaneous transfer of four electrons is unlikely. Indeed, Ammar et al. [7] proposed a single electron transfer slow step for the reduction of MTZ at boron doped diamond, as illustrated in Eq. (6). The heterogenous rate constant k^0 was computed using Eq. (7), where F, A, C, R, T and F have their usual meanings [25]. The E^0 value was estimated by extrapolating ν to 0 using a plot of E_p as a function of the logarithm of ν. Considering a one-electron transfer rate determining step, the k^0 value was computed as 2.5 × 10^{-3} s^{-1} m^3 mol^{-1} for GCE/Gr/Bi. This indicates an efficient reduction of MTZ at the GCE/Gr/Bi. The corresponding linear plot is depicted in Fig. S2 (supplementary data), with a linear regression equation of lnI_p = −34.25(E_p − E^0) −14.97, R^2 = 0.986.

$$E_p - E_{p1/2} = \frac{47.7}{n'\alpha} \qquad (5)$$

$$R\text{–}NO_2 + e^- \rightarrow R\text{–}NO_2^- \text{ (slow step)} \qquad (6)$$

$$I_p = 0.277nFACk^o e^{-(\alpha n F(E_p - E^0))/RT} \qquad (7)$$

3.3. Influence of pH and the nature of the deposited Bi

As illustrated in Scheme 1, the reduction of MTZ involves the reduction of the NO_2 group to form NHOH, and this reaction involves the participation of hydrogen ions. Accordingly, the pH of the solution will influence the position of the reduction wave and this is evident in Fig. 4(a). In these experiments, the pH of a 4.0 mM MTZ solution was varied from a pH of 4.0–12.0 and the corresponding voltammograms recorded for the GCE/Bi sensor are shown in Fig. 4(a), This high concentration of MTZ was employed so that the pH data could be compared with the unmodified GCE, which exhibits a weak signal, as illustrated in Fig. 1(b). The corresponding relationship between the peak potential and pH is illustrated in Fig. 4(b). As the pH is increased from 4.0 to 12.0, there is clear shift in the peak potential to lower values and this is consistent with the participation of H^+ ions in the reduction process, as illustrated in Scheme 1. It is also evident from Fig. 4(a) that an oxidation wave emerges as the pH is increased and this becomes more evident as the pH is increased beyond a pH of 9.0. This can be explained in terms of the formation of bismuth oxides. According to the Pourbaix diagram of Bi, the Bi_2O_3 phase becomes thermodynamically stable at potentials in the vicinity of 0.0–0.8 V (SHE) and at pH values higher than about 9.0. The conversion of Bi to Bi_2O_3 can be described by Eq. (2), while the corresponding relationship between the electrode potential and pH is given in Eq. (3). Using Eq. (3), it is seen that E will become lower as the pH is increased. At a pH of 9.0, $E = -0.161$ V (SHE), which is equivalent to -0.401 V on the SCE scale and this is in very good agreement with the oxidation waves observed in Fig. 4(a). Furthermore, the peak potential shifts to lower potentials with increasing pH and this agrees well with Eq. (3). The oxidation peak at a pH of 12 is somewhat lower and this is probably related to the solubilisation of Bi_2O_3 in this highly alkaline solution.

$$2Bi + 3H_2O \rightarrow Bi_2O_3 + 6H^+ + 6e^- \qquad (2)$$

$$E = 0.371\text{–}0.0591 \text{ pH} \qquad (3)$$

The influence of pH on the peak current is illustrated in Fig. 4(b) for the GCE/Bi and GCE electrodes, respectively. The relationship is very different with the two electrodes. With the GCE electrode, the highest peak current is observed at a pH of 6.0 and this is in very good agreement with several studies [10]. On the other hand, the highest peak current is observed at a pH of 12.0 for the GCE/Bi, indicating a higher rate of electron transfer in the alkaline solution. This may be connected to the in-situ formation of Bi_2O_3 which becomes the thermodynamically stable phase at pH values higher than 9.0.

The influence of pH on the peak potential is more clearly shown in Fig. 4(c), where two linear regions become evident. The equation of the linear region between a pH of 4.0 and 9.0 was deduced as $E = -0.0487$ pH $- 0.2340$, $R^2 = 0.993$, with good linearity. The slope of 0.0487 V/pH is reasonably close to the theoretical value of $0.0591(m/n)$ V/pH obtained from the Nernst equation at 298 K, where m represents the number of protons transferred and n corresponds to the number of electrons involved in the electron-transfer step. Although, there is some deviation from the theoretical slope, the m/n value was computed as 0.83, which is consistent with the participation of equal numbers of protons and electrons during the electron transfer step. However, as the pH is further increased from 9.0 to 12.0, the relationship becomes $E = -0.0240$ pH $- 0.4561$ and a lower slope is observed as the H^+ concentration is diminished. Again, this may be related to the formation of bismuth oxides, which become the thermodynamically favoured phase at pH values of 9.0 and higher.

Evidence for the formation of bismuth oxides at pH values higher than 9.0 was obtained using FTIR. Typical spectra are shown in Fig. 4(d), where the spectrum recorded for the freshly prepared GCE/Bi is compared with the GCE/Bi cycled in a pH 10.0 buffer. The electrodeposited Bi has a weak peak at 1382 cm^{-1} which may be related to adsorbed nitrates, or Bi–OH, but there is no evidence of any oxide phases. However, when the Bi is cycled in a buffer at a pH of 10.0, additional peaks emerge and these can be explained in terms of the
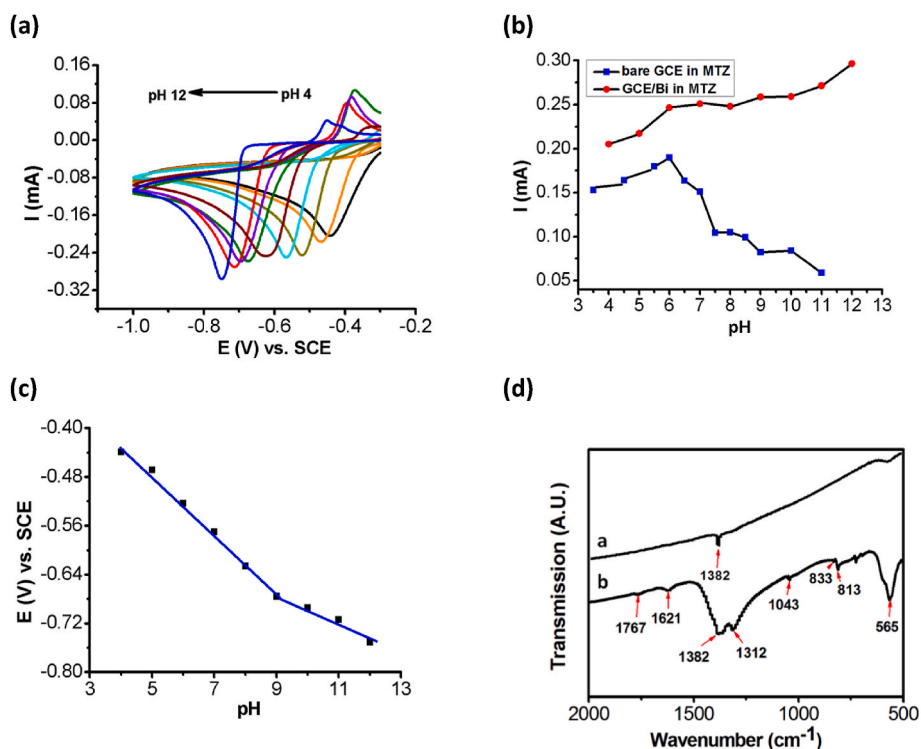

Fig. 4. (a) CVs of GCE/Bi in 4.0 mM MTZ in PBS with different pH values, **(b)** peak currents as a function of pH values for GCE and GCE/Bi electrodes, **(c)** peak potentials versus pH and **(d)** FTIR spectra of GCE/Bi (a) freshly deposited and (b) cycled in a pH 10 buffer solution.

formation of bismuth oxides and are in good agreement with data previously recorded for Bi_2O_3 [26]. In particular, the peaks observed at 813, 833 and 1043 cm^{-1} can be attributed to the stretching of bismuth oxides [26], while the peak at 565 cm^{-1} can be assigned to the Bi–O–Bi stretching vibration. The stronger bands at 1312 and 1382 cm^{-1} are consistent with the presence of Bi–OH [27], while the weak band at 1621 cm^{-1} is probably due to the bending vibration of adsorbed water molecules.

3.4. Sensitivity, selectivity and water analysis

Studies on the performance of the fabricated GCE/Gr/Bi sensor in the detection of MTZ were carried out by varying the concentration of MTZ. Representative data are shown in Fig. 5(a), where the cyclic voltammograms are presented for a series of MTZ concentrations between 0.005 and 260 μM, while the inset shows the data recorded for concentrations from 5 to 120 nM. At these lower concentrations, the MTZ reduction peaks appear more symmetrical, while the small reversible redox waves evident at about −0.45 V vs SCE can be attributed to oxygenated species at the Gr nanoplates. When the peak current was plotted as a function of concentration, a linear plot was obtained, as shown in Fig. 5(b). With linear regression analysis, the equation, I (mA) $= 0.6487c$ (mM) $+ 0.0047$, $R^2 = 0.995$, was obtained, indicating excellent linearity over a wide concentration region. The calibration curve obtained with nM concentrations is shown in the inset in Fig. 5(b), and again very good linearity is achieved. Using the well-known relationship for the limit of detection (LOD $= 3\sigma$/sensitivity), where σ corresponds to the standard deviation in the current signal in the absence of the MTZ, the LOD was calculated as 0.90 nM. This gives a low LOD value combined with a sensitivity of 0.65 μA/μM. Using a similar approach, the linear regression equation was obtained as I (mA) $= 0.1780c$ (mM) $+ 0.02674$, $R^2 = 0.9953$ for the GCE/Bi. Again, excellent linearity was observed, however in this case the computed LOD was higher at 3.3 nM and the sensitivity was lower adopting a value of 0.18 μA/μM. This comparison clearly illustrates that enhanced detection is possible using both Gr and Bi. This may be connected to the adsorption of MTZ at the Gr nanoplatelets and the higher electroactive surface area of the GCE/Gr/Bi.

In terms of typical concentrations of MTZ found in the environment, it has been reported that the levels can range from 0.5 to 21.4 ng/L in drinking water, but are higher in river sediments, reaching levels of 1.21 μg/kg and ranging from 6.3 to 27.2 μg/kg in vegetables [28]. While the LOD of 0.90 nM may not be suitable for direct analysis of drinking water, the linear range is suitable for levels found in vegetables and sediments. A comparison of the GCE/Gr/Bi and GCE/Bi sensors with some previously reported sensors for the analysis of MTZ is made in Table 2, focussing on the more recent reports. In many of these studies, two linear concentration ranges are evident and for this comparison the lower concentration ranges, which have been used by the authors to compute the LOD values, are only provided. Here it is evident that the

Table 2
Comparison of sensors in the electrochemical detection of MTZ.

Sensor materials[a]	Technique[a]	Linear range/ μM	LOD/ nM	Reference
CNF@AuNPs	DPV	0.1–100	24	[29]
C60-rGO-NF/SPE	SWV	0.25–34	210	[8]
CdS QDs	DPV	0.1–203	53	[9]
Ni/Fe-LDH	Amperometry	5–161	58	[30]
Dy(VO_4)/f-CNF/SPCE	LSV	1.5–1036	6	[6]
ZnV MS	DPV	0.05–59	9	[31]
ZnCo-based metal-organic framework	LSV	0.05–100	17	[32]
N, S, P- porous carbon	LSV	0.1–45	13	[33]
DyM/GCE	DPV	0.01–2363	3	[34]
αFe_2O_3/CPE	CV	0.8–100	285	[35]
O-gCN/GCE	DPV	0.01–2060	5	[36]
MWNT-CS-Ni/GCE	DPV	0.1–150	25	[37]
NiO/Ni	DPV	0.01–1.63	6	[38]
AgNP/CuMOF/ PPy–rGO	SWV	0.08–160	24	[39]
μAl_2O_3/CPE	DPV	0.5–1000	253	[40]
GCE/Bi	CV	0.02–240	3	This work
GCE/Gr/Bi	CV	0.005–260	0.9	This work

[a] DPV – differential pulse voltammetry; LSV – linear sweep voltammetry; SWV – square wave voltammetry; AuPNs – gold nanoparticles; CS – chitosan; g-CN – graphitic carbon nitride; LDH – layered double hydroxide; MOF – metal organic framework; MWCNT – multiwalled carbon nanotubes; MS – microstructures; PPy – polypyrrole; QDs – quantum dots; rGO – reduced graphene; SPE – screen printed electrode.

GCE/Gr/Bi compares well in terms of the LOD and linear concentration range. However, it is the simplicity of the GCE/Gr/Bi sensor that makes it suitable for the electrochemical detection of MTZ, especially in terms of water analysis.

The selectivity was studied using a variety of interfering compounds, including inorganic salts that are present in aquatic environments and also some organic compounds, such as glucose. The interferents included additional phosphates (KH_2PO_4), cations including Mg^{2+} ($MgCl_2$), Zn^{2+} ($ZnCl_2$), Ca^{2+} ($CaCl_2$), NH_4Cl (AC) to give NH_4^+ cations, sulfates (Na_2SO_4), nitrates ($NaNO_3$), carbonates (Na_2CO_3), chlorides ($CaCl_2$), and citrates (CA). In addition, nitrophenols, (ortho- and *para*-nitrophenol, o-NP and p-NP) and hydrocortisone (HC) were selected as interferents as these can be electrochemically reduced at a similar potential as MTZ. The interference study was recorded using cyclic voltammetry in a 0.1 mM MTZ solution dissolved in a neutral phosphate buffer. The interferents were added at a concentration of 1.0 mM for the inorganic ions and glucose, to give a 10-fold excess over the concentration of MTZ, while the concentrations of o-NP, p-NP, and HC, were 0.1 mM. The normalised reduction peak currents (I/I_0, where I is the peak current in the presence of the interferent and I_0 is the peak current in the absence of the interferent) are summarised in Fig. 6(a). It is evident that the peak currents are nearly identical, except on the addition of nitrates and o-NP, where there is an increase in the current. This
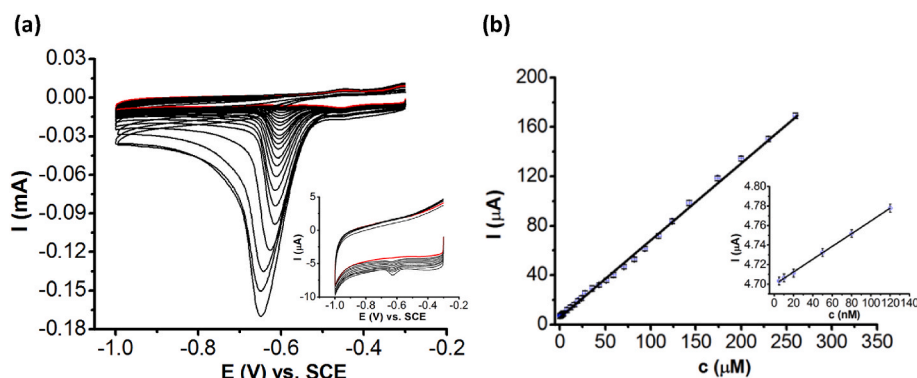

(a)

(b)

Fig. 5. (a) CVs of GCE/Gr/Bi recorded at 50 mV s^{-1} in MTZ at concentrations from 0.005 to 260 μM with inset showing CVs at concentrations between 5 nM and 120 nM; the red curve shows the CV of GCE/Gr/Bi recorded at 50 mV s^{-1} in PBS (blank); **(b)** peak current plotted as a function of the MTZ concentration, with inset showing the concentration range from 5 to 120 nM. (For interpretation of the references to colour in this figure legend, the reader is referred to the Web version of this article.)
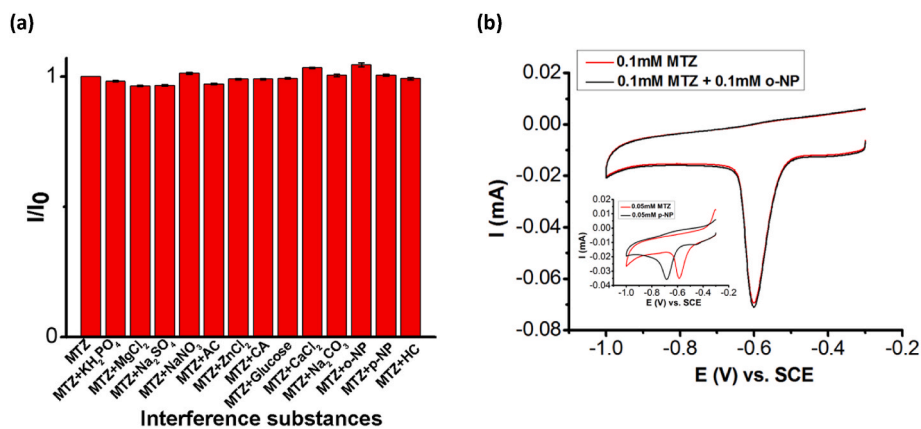
Fig. 6. (a) Normalised peak currents, (I/I_0), of 0.1 mM MTZ at GCE/Gr/Bi in a phosphate buffer solution containing 10-fold concentrations of various inorganic ions and glucose, and with equimolar concentrations of organic compounds (phenols and HC), **(b)** 0.1 mM MTZ in the presence and absence of 0.1 mM o-NP at GCE/Gr/Bi and the inset shows CVs recorded in 0.05 mM MTZ and also in 0.05 mM p-NP.

is consistent with the reduction of nitrates and o-NP at the modified electrode, but the interference is low giving a 1.3% increase in the peak current. The addition of sulfates, chlorides, carbonates and phosphate salts that are frequently found in aquatic environments have little influence on the peak current. These are not electroactive, but may adsorb at the electrode surface in competition with the adsorption of MTZ at GCE/Gr/Bi. However, the adsorption of MTZ is not affected by these interferents. While the reduction of o-NP occurs at a potential similar to that of MTZ and gives rise to an increase in the peak current, Fig. 6(b), the reduction of p-NP occurs at a lower potential than MTZ. As shown in the inset of Fig. 6(b), the reduction of p-NP occurs with a significant peak current at the GCE/Gr/Bi surface, but the reduction waves associated with MTZ and p-NP are well separated and as illustrated in Fig. 6 (a) p-NP is not an interferent in the electrochemical detection of MTZ.

The performance of the sensor in the analysis of MTZ in tap water was studied using a typical spiking and recovery experiment. Tap water was spiked with different concentrations of MTZ and the recovery was analysed using the GCE/Gr/Bi. For comparison purposes, deionised water was also employed. The data obtained are summarised in Table 3 where it is seen that good recovery is achieved in the tap water, with the recovery varying between 101.36 and 97.95%. These recovery values are similar to that observed using deionised water, indicating good performance of the GCE/Gr/Bi sensor.

3.5. Stability and regeneration of the sensor

The stability of the sensors was studied using cyclic voltammetry, where the peak current was recorded following repeated cycling. The peak currents are presented as a function of the cycle number under stationary and mild stirring conditions for the GCE/Bi and GCE/Gr/Bi in Fig. 7(a). There is no evidence of any electrode fouling even at this elevated 4 mM MTZ concentration and the peak currents remain essentially constant over the 40 cycles. Although not shown, significant fouling was observed with the unmodified GCE. In addition, the mild

stirring (at 100 rpm) enhances the diffusion of MTZ and this is reflected in higher peak currents that also remain constant over the cycling period.

One significant advantage of employing the electrodeposited bismuth films is the possibility of easy regeneration of the bismuth layer. This was explored using two approaches. Firstly, the bismuth layer at the GCE/Gr/Bi was oxidised and removed from the surface by applying a potential of 0.60 V vs SCE for 400 s. Then a freshly deposited bismuth layer was applied at −1.0 V vs SCE for 100 s. This oxidation and regeneration step was repeated five times and the resulting voltammograms are depicted in Fig. 7(b). Here, it is evident that good repeatability is achieved with a 0.5% error in the peak currents. Secondly, regeneration of the bismuth layer was attempted using an in-situ method, where the Bi(III) was added to the MTZ-containing solution, while the modified electrode was cycled to 0.0 V vs SCE to remove the previously deposited Bi layer. The MTZ solution was adjusted to a pH of 1.23 to avoid the precipitation of insoluble bismuth hydroxides. As a result, the reduction wave of MTZ was shifted to more positive potentials to coincide with the reduction wave associated with the Bi(III) reduction. Nevertheless, this peak, now arising from the reduction of Bi(III) and MTZ, is sensitive to the MTZ concentration, as illustrated in Fig. 7(c) and (d). This analysis clearly shows that the bismuth layer can be regenerated either through an ex-situ or in-situ approach. The ex-situ method provides very good reproducibility and appears as the more promising approach with a 100 s regeneration step without the requirement to acidify the analyte.

4. Conclusion

A simple and effective sensor for the electrochemical detection of metronidazole was fabricated through a facile electrodeposition process, where Gr nanoplatelets were initially deposited onto the glassy carbon electrode followed by a 1 min electrodeposition of Bi from an acidified Bi(III) solution. The Bi was well dispersed across the surface and the resulting GCE/Gr/Bi performed well to give a linear concentration range, good selectivity, good recovery and a low LOD value. Nevertheless, it is the simplicity of the sensor fabrication process coupled with the ability to readily regenerate the Bi deposits that makes this an interesting sensor. Indeed, this simple approach could be employed in the analysis of other analytes, where the generation of a new clean surface is important.

Credit author statement

T. Yu – Conceptualisation, methodology, validation, formal analysis, investigation, funding acquisition, writing - review & editing; L. Glennon – Investigation, conceptualisation, writing; O Fenelon –
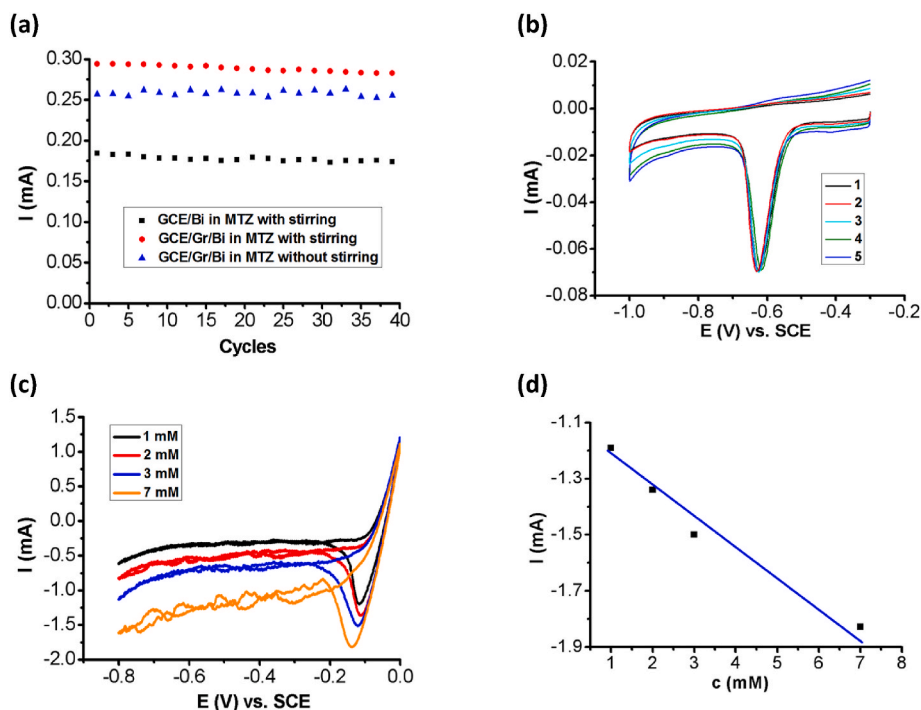
Table 3
Determination of MTZ in deionised water and tap water using GCE/Gr/Bi. Sufficient phosphate was added to the deionised and tap water samples to give a 0.1 M phosphate solution.

Sample	Added/μM	Found/μM	Recovery
Deionised water	10.0	10.17	101.7%
	50.0	49.22	98.44%
	100.0	102.15	102.15%
Tap water	10.0	9.86	98.6%
	50.0	50.68	101.36%
	100.0	97.95	97.95%

Fig. 7. (a) Peak currents of MTZ (4 mM) plotted as a function of CV cycle number with and without stirring, **(b)** CVs of MTZ using the regenerated Bi layers at GCE/Gr/Bi in 0.1 mM MTZ, **(c)** CVs recorded for GCE in a mixture of MTZ (1–7 mM) and Bi(NO$_3$)$_3$ (5 mM) and **(d)** peak current as a function of the MTZ concentration in Fig. 7(c).

Investigation, methodology; C.B. Breslin – Supervision, funding acquisition, writing - original draft, writing - review & editing, visualisation.

Declaration of competing interest

The authors declare that they have no known competing financial interests or personal relationships that could have appeared to influence the work reported in this paper.

Acknowledgements

Appendix A. Supplementary data

Supplementary data to this article can be found online at https://doi.org/10.1016/j.talanta.2022.123758.

References

[1] P. Malfertheiner, F. Megraud, C. O'Morain, F. Bazzoli, E. El-Omar, D. Graham, R. Hunt, T. Rokkas, N. Vakil, E.J. Kuipers, L. Andersen, J. Atherton, M. Asaka, F. Bazzoli, P. Bytzer, F. Chan, L.G. V Coelho, N. De Wit, J.C. Delchier, F. Di Mario, E. El-Omar, K.M. Fock, D. Forman, T. Fujioka, G. Gasbarrini, R. Genta, K.L. Goh, D. Y. Graham, A. Hirschl, P. Hungin, R. Hunt, V.A. Isakov, R. Jones, M. Kist, S. Koletzko, E.J. Kuipers, L. Kupcinskas, S. Ladas, A. Lanas, J. Machado, P. Malfertheiner, K.E.L. McColl, F. Mégraud, P. Michetti, P. Moayyedi, C. Omorain, A. Pilotto, M. Quina, T. Rokkas, P. Sharma, Y. Simsek, P. Sipponen, J. Sollano, R. Stockbrügger, K. Sugano, D. Vaira, N. Vakil, M. Vieth, S. Xiao, Current concepts in the management of helicobacter pylori infection: the maastricht III consensus report, Gut 56 (2007) 772–781, https://doi.org/10.1136/gut.2006.101634.
[2] C.D. Freeman, N.E. Klutman, K.C. Lamp, Metronidazole. A therapeutic review and update, Drugs 54 (1997) 679–708, https://doi.org/10.2165/00003495-199754050-00003.
[3] A. Hernández Ceruelos, L.C. Romero-Quezada, J.C. Ruvalcaba Ledezma, L. López Contreras, Therapeutic uses of metronidazole and its side effects: an update, Eur. Rev. Med. Pharmacol. Sci. 23 (2019) 397–401, https://doi.org/10.26355/eurrev_201901_16788.
[4] D.J. Quincey, P. Kay, J. Wilkinson, L.J. Carter, L.E. Brown, High concentrations of pharmaceuticals emerging as a threat to Himalayan water sustainability, Environ. Sci. Pollut. Res. 29 (2022) 16749–16757, https://doi.org/10.1007/s11356-021-18302-8.
[5] H. Wang, D. Qian, X. Xiao, C. Deng, L. Liao, J. Deng, Y.-W. Lin, Preparation and application of a carbon paste electrode modified with multi-walled carbon nanotubes and boron-embedded molecularly imprinted composite membranes, Bioelectrochemistry 121 (2018) 115–124, https://doi.org/10.1016/j.bioelechem.2018.01.006.
[6] B. Muthukutty, B. Arumugam, S.-M. Chen, S.K. Ramaraj, Low potential detection of antiprotozoal drug metronidazole with aid of novel dysprosium vanadate incorporated oxidized carbon nanofiber modified disposable screen-printed electrode, J. Hazard Mater. 407 (2021), 124745, https://doi.org/10.1016/j.jhazmat.2020.124745.
[7] H.B. Ammar, M.B. Brahim, R. Abdelhédi, Y. Samet, Boron doped diamond sensor for sensitive determination of metronidazole: mechanistic and analytical study by cyclic voltammetry and square wave voltammetry, Mater. Sci. Eng. C 59 (2016) 604–610, https://doi.org/10.1016/j.msec.2015.10.025.
[8] E.M. Materón, A. Wong, T.A. Freitas, R.C. Faria, O.N. Oliveira, A sensitive electrochemical detection of metronidazole in synthetic serum and urine samples using low-cost screen-printed electrodes modified with reduced graphene oxide and C60, J. Pharm. Anal. 11 (2021) 646–652, https://doi.org/10.1016/j.jpha.2021.03.004.
[9] P.K. Gopi, P. Kesavan, G. Kesavan, S.-M. Chen, C.H. Ravikumar, Cadmium sulfide quantum dots anchored on reduced graphene oxide for the electrochemical detection of metronidazole, New J. Chem. 45 (2021) 3022–3033, https://doi.org/10.1039/d0nj05501h.
[10] V. Velusamy, S. Palanisamy, T. Kokulnathan, S.-W. Chen, T.C.K. Yang, C.E. Banks, S.K. Pramanik, Novel electrochemical synthesis of copper oxide nanoparticles decorated graphene-β-cyclodextrin composite for trace-level detection of antibiotic drug metronidazole, J. Colloid Interface Sci. 530 (2018) 37–45, https://doi.org/10.1016/j.jcis.2018.06.056.
[11] S. Chinnaraj, V. Palani, S. Yadav, M. Arumugam, M. Sivakumar, V. Maluventhen, M. Singh, Green synthesis of silver nanoparticle using goniothalamus wightii on graphene oxide nanocomposite for effective voltammetric determination of metronidazole, Sens. Bio-Sensing Res. 32 (2021), 100425, https://doi.org/10.1016/j.sbsr.2021.100425.
[12] A.K. Vivekanandan, V. Subash, S.-M. Chen, S.-H. Chen, Sonochemical synthesis of nickel-manganous oxide nanocrumbs decorated partially reduced graphene oxide for efficient electrochemical reduction of metronidazole, Ultrason. Sonochem. 68 (2020), 105176, https://doi.org/10.1016/j.ultsonch.2020.105176.
[13] S.B. Hočevar, B. Ogorevc, J. Wang, B. Pihlar, A study on operational parameters for advanced use of bismuth film electrode in anodic stripping voltammetry, Electroanalysis 14 (2002) 1707–1712, https://doi.org/10.1002/elan.200290014.
[14] A. Królicka, R. Pauliukaitappproaches the limit, I. Svancara, R. Metelka, A. Bobrowski, E. Norkus, K. Kalcher, K. Vytřas, Bismuth-film-plated carbon paste

electrodes, Electrochem. Commun. 4 (2002) 193–196, https://doi.org/10.1016/S1388-2481(01)00301-0.

[15] I. Švancara, L. Baldrianová, E. Tesařová, S.B. Hočevar, S.A.A. Elsuccary, A. Economou, S. Sotiropoulos, B. Ogorevc, K. Vytřas, Recent advances in anodic stripping voltammetry with bismuth-modified carbon paste electrodes, Electroanalysis 18 (2006) 177–185, https://doi.org/10.1002/elan.200503391.

[16] H. Zhang, J. Cui, Y. Zeng, Y. Zhang, Y. Pei, Direct electrodeposition of carbon dots modifying bismuth film electrode for sensitive detection of Cd^{2+} and Pb^{2+}, J. Electrochem. Soc. 169 (2022), 017501 https://doi.org/10.1149/1945-7111/ac47e7.

[17] H. Li, J. Zhao, S. Zhao, G. Cui, Simultaneous determination of trace Pb(II), Cd(II), and Zn(II) using an integrated three-electrode modified with bismuth film, Microchem. J. 168 (2021), https://doi.org/10.1016/j.microc.2021.106390.

[18] S.E.D. Bahinting, A.P. Rollon, S. Garcia-Segura, V.C.C. Garcia, B.M.B. Ensano, R.R. M. Abarca, J.-J. Yee, M.D.G. de Luna, Bismuth film-coated gold ultramicroelectrode array for simultaneous quantification of Pb(II) and Cd(II) by square wave anodic stripping voltammetry, Sensors 21 (2021) 1–19, https://doi.org/10.3390/s21051811.

[19] N. Lezi, A. Economou, J. Barek, M. Prodromidis, Screen-printed disposable sensors modified with bismuth precursors for rapid voltammetric determination of 3 ecotoxic nitrophenols, Electroanalysis 26 (2014) 766–775, https://doi.org/10.1002/elan.201400001.

[20] B. Singh, A. Singh, A. Sharma, P. Mahajan, S. Verma, B. Padha, A. Ahmed, S. Arya, Electrochemical sensing and photocatalytic degradation of 2,4-dinitrophenol via bismuth(III) oxide nanowires, J. Mol. Struct. 1255 (2022), 132379, https://doi.org/10.1016/j.molstruc.2022.132379.

[21] F. Franceschini, M. Bartoli, A. Tagliaferro, S. Carrara, Electrodes for paracetamol sensing modified with bismuth oxide and oxynitrate heterostructures: an experimental and computational study, Chemosensors 9 (2021) 361, https://doi.org/10.3390/chemosensors9120361.

[22] M. Yang, Z. Hu, Electrodeposition of bismuth onto glassy carbon electrodes from nitrate solutions, J. Electroanal. Chem. 583 (2005) 46–55, https://doi.org/10.1016/j.jelechem.2005.04.019.

[23] E.A. Hutton, B. Ogorevc, S.B. Hočevar, F. Weldon, M.R. Smyth, J. Wang, An introduction to bismuth film electrode for use in cathodic electrochemical detection, Electrochem. Commun. 3 (2001) 707–711, https://doi.org/10.1016/S1388-2481(01)00240-5.

[24] M. Mohammadi, A. Tavajjohi, A. Ziashahabi, N. Pournoori, S. Muhammadnejad, H. Delavari, R. Poursalehi, Toxicity, morphological and structural properties of chitosan-coated Bi_2O_3-$Bi(OH)_3$ nanoparticles prepared via DC arc discharge in liquid: a potential nanoparticle-based CT contrast agent, Micro & Nano Lett. 14 (2019) 239–244, https://doi.org/10.1049/mnl.2018.5145.

[25] K. Balamurugan, R. Karthik, S.-M. Chen, R. Sukanya, B. Thasma Subramanian, V. M.N. Biju, J.-J. Shim, C.B. Breslin, Heterostructures of mixed metal oxides ($ZnMnO_3$/ZnO) synthesized by a wet-chemical approach and their application for the electrochemical detection of the drug chlorpromazine, Compos. B Eng. 236 (2022) 109822, https://doi.org/10.1016/j.compositesb.2022.109822.

[26] Y. Azizian-Kalandaragh, F. Sedaghatdoust-Bodagh, A. Habibi-Yangjeh, Ultrasound-assisted preparation and characterization of β-Bi_2O_3 nanostructures: exploring the photocatalytic activity against rhodamine B, Superlattice. Microst. 81 (2015) 151–160, https://doi.org/10.1016/j.spmi.2014.12.038.

[27] M.A. Hobosyan, S.A. Yolchinyan, K.S. Martirosyan, A novel nano-energetic system based on bismuth hydroxide, RSC Adv. 6 (2016) 66564–66570, https://doi.org/10.1039/c6ra12854h.

[28] N. Hanna, P. Sun, Q. Sun, X. Li, X. Yang, X. Ji, H. Zou, J. Ottoson, L.E. Nilsson, B. Berglund, O.J. Dyar, A.J. Tamhankar, C. Stålsby Lundborg, Presence of antibiotic residues in various environmental compartments of Shandong province in eastern China: its potential for resistance development and ecological and human risk, Environ. Int. 114 (2018) 131–142, https://doi.org/10.1016/j.envint.2018.02.003.

[29] L. Zhang, M. Yin, J. Qiu, T. Qiu, Y. Chen, S. Qi, X. Wei, X. Tian, D. Xu, An electrochemical sensor based on CNF@AuNPs for metronidazole hypersensitivity detection, Biosens. Bioelectron. X. 10 (2022), 100102, https://doi.org/10.1016/j.biosx.2021.100102.

[30] K. Nejati, K. Asadpour-Zeynali, Electrochemical synthesis of nickel-iron layered double hydroxide: application as a novel modified electrode in electrocatalytic reduction of metronidazole, Mater. Sci. Eng. C 35 (2014) 179–184, https://doi.org/10.1016/j.msec.2013.11.003.

[31] G. Kesavan, S.-M. Chen, Sonochemical-assisted synthesis of zinc vanadate microstructure for electrochemical determination of metronidazole, J. Mater. Sci. Mater. Electron. 32 (2021) 9377–9391, https://doi.org/10.1007/s10854-021-05601-6.

[32] Y. Baikeli, X. Mamat, M. Wumaer, M. Muhetaer, H.A. Aisa, G. Hu, Electrochemical determination of metronidazole using a glassy carbon electrode modified with nanoporous bimetallic carbon derived from a ZnCo-based metal-organic framework, J. Electrochem. Soc. 167 (2020), 116513, https://doi.org/10.1149/1945-7111/ab9d94.

[33] N. Yalikun, X. Mamat, Y. Li, X. Hu, P. Wang, G. Hu, N, s, p-triple doped porous carbon as an improved electrochemical sensor for metronidazole determination, J. Electrochem. Soc. 166 (2019), https://doi.org/10.1149/2.0321913jes. B1131–B1137.

[34] R. Karthik, B. Mutharani, S.-M. Chen, J. Vinoth Kumar, M. Abinaya, T.-W. Chen, W. Lei, Q. Hao, Synthesis, characterization and catalytic performance of nanostructured dysprosium molybdate catalyst for selective biomolecule detection in biological and pharmaceutical samples, J. Mater. Chem. B. 7 (2019) 5065–5077, https://doi.org/10.1039/c9tb01020c.

[35] J. Zoubir, N. Bougdour, C. Radaa, A. Idlahcen, I. Bakas, A. Assabbane, Elaboration of a novel nanosensor using nanoparticles of α-Fe_2O_3 magnetic cores for the detection of metronidazole drug. Urine human and tap water, Sensors Int 3 (2022), 100160, https://doi.org/10.1016/j.sintl.2022.100160.

[36] G. Kesavan, V. Vinothkumar, S.-M. Chen, T.D. Thangadurai, Construction of metal-free oxygen-doped graphitic carbon nitride as an electrochemical sensing platform for determination of antimicrobial drug metronidazole, Appl. Surf. Sci. 556 (2021), https://doi.org/10.1016/j.apsusc.2021.149814.

[37] A. Mao, H. Li, L. Yu, X. Hu, Electrochemical sensor based on multi-walled carbon nanotubes and chitosan-nickel complex for sensitive determination of metronidazole, J. Electroanal. Chem. 799 (2017) 257–262, https://doi.org/10.1016/j.jelechem.2017.05.049.

[38] M. Darbandi, M.F. Mohajer, M. Eynollahi, K. Asadpour-Zeynali, Sensitive sensing platform based on NiO and NiO-Ni nanoparticles for electrochemical determination of Metronidazole, Chem. Phys. 560 (2022), 111590, https://doi.org/10.1016/j.chemphys.2022.111590.

[39] H. Saedi, M.R. Fat'hi, B. Zargar, Synthesis of AgNPs functionalized CuMOF/PPy–rGO nanocomposite and its use as an electrochemical sensor for metronidazole determination, J. Chin. Chem. Soc. 68 (2021) 1954–1964, https://doi.org/10.1002/jccs.202100081.

[40] J. Zoubir, C. Radaa, A. Idlahcen, I. Bakas, A. Assabbane, A new voltammetric sensor for metronidazole based on electro catalytic effect of Al_2O_3 modified carbon graphite. Application. Urine, tap water and river water, Mater. Sci. Energy Technol. 4 (2021) 296–306, https://doi.org/10.1016/j.mset.2021.08.003.